PNAS RESEARCH ARTICLE | PLANT BIOLOGY

Arabidopsis protein *S*-acyl transferases positively mediate BR signaling through *S*-acylation of BSK1

Fei Liu[a], Peng-Yu Qu[a], Ji-Peng Li[b], Li-Na Yang[b], Yuan-Jun Geng[b], Jin-Yu Lu[a], Yan Zhang[a,1], and Sha Li[b,1]

Edited by Mark Estelle, University of California at San Diego, La Jolla, CA; received December 27, 2023; accepted January 5, 2024

Protein *S*-acyl transferases (PATs) catalyze *S*-acylation, a reversible post-translational modification critical for membrane association, trafficking, and stability of substrate proteins. Many plant proteins are potentially *S*-acylated but few have corresponding PATs identified. By using genomic editing, confocal imaging, pharmacological, genetic, and biochemical assays, we demonstrate that three Arabidopsis class C PATs positively regulate BR signaling through *S*-acylation of BRASSINOSTEROID-SIGNALING KINASE1 (BSK1). PAT19, PAT20, and PAT22 associate with the plasma membrane (PM) and the *trans*-Golgi network/early endosome (TGN/EE). Functional loss of all three genes results in a plethora of defects, indicative of reduced BR signaling and rescued by enhanced BR signaling. PAT19, PAT20, and PAT22 interact with BSK1 and are critical for the *S*-acylation of BSK1, and for BR signaling. The PM abundance of BSK1 was reduced by functional loss of *PAT19*, *PAT20*, and *PAT22* whereas abolished by its *S*-acylation-deficient point mutations, suggesting a key role of *S*-acylation in its PM targeting. Finally, an active BR analog induces vacuolar trafficking and degradation of PAT19, PAT20, or PAT22, suggesting that the *S*-acylation of BSK1 by the three PATs serves as a negative feedback module in BR signaling.

brassinosteroids | hypocotyl | plasma membrane | root apical meristem | stomatal development

Significance

Brassinosteriods (BRs) are plant hormones mediating various developmental processes. BSK1 relays BR signaling by interacting with the BR receptor BRI1 and phosphorylating downstream targets. Plasma membrane-association of BSK1 relies on *S*-acylation, a reversible post-translational modification catalyzed by protein S-acyl transferases (PATs). This study identifies Arabidopsis PAT19, PAT20, and PAT22 for BSK *S*-acylation, for BR signaling, and for plant development. In turn, BR signaling initiates vacuolar degradation of these PATs, providing a negative feedback module for BR-mediated growth.

Protein *S*-acylation is a reversible post-translational modification commonly referred to as palmitoylation, which usually involves the addition of a 16-carbon saturated palmitate group to the sulfhydryl group of a cysteine (Cys) to form a thioester (1, 2). *S*-acylation facilitates membrane association of soluble proteins, affects trafficking of endomembrane proteins, and influences their interactomes or stability (2–5). Protein *S*-acyl transferases (PATs) are major enzymes to catalyze protein *S*-acylation, encoded by multiple genes in all plant genomes (6). A few Arabidopsis PATs were functionally characterized and they mediate tip growth, reproduction, development, and responses to abiotic and biotic stresses (3, 4, 7–15).

A large number of Arabidopsis proteins have been experimentally demonstrated or predicted to be *S*-acylated, including small GTPases, SNARE proteins, receptor-like cytoplasmic kinases (RLCKs), and receptor-like kinases (RLKs) (1, 16). However, few PAT-substrate pairs are known. In Arabidopsis, several calcineurin B-like (CBL) proteins were *S*-acylated by PAT10 (4, 17); two disease-responsive proteins were *S*-acylated by PAT5 and PAT9 or PAT13 and PAT16, respectively (15, 18). Despite these progresses, the identification of PAT-substrate pairs is hindered by a high redundancy of plant PATs and the lack of consensus motifs for *S*-acylation.

The phytohormone brassinosteroids (BR) are critical for cell growth and division, playing essential roles in plant development (19, 20). BRs are sensed at the plasma membrane (PM) by BRASSINOSTEROID-INSENSITIVE 1 (BRI1) and its co-receptor BRI1-ASSOCIATED RECEPTOR KINASE 1 (BAK1). BRI1 and BAK1 subsequently phosphorylate each other and activate BRASSINOSTEROID-SIGNALING KINASE1 (BSK1) and CONSTITUTIVE DIFFERENTIAL GROWTH1 (CDG1) (21–23). BSK1 and CDG1 interact with the phosphatase BRI1 SUPPRESSOR1 (BSU1) to inhibit the activity of BIN2 and by doing so promotes BRASSINAZOLE RESISTANT1 (BZR1)-dependent transcription for most BR responses (19, 24).

BSK1 and CDG1 are RLCKs, which often relay signals from RLKs to cytoplasmic targets through phosphorylation cascades (22). Unlike RLKs that contain transmembrane domains, RLCKs often associate with the PM through lipid modifications, such as *N*-myristoylation and *S*-acylation (25). Mutations of two Cys residues in CDG1 to Ala, presumably abolishing its *S*-acylation sites, resulted in the mis-targeting of CDG1 to the nuclei (23). A G2A mutation (the second amino acid Gly mutated to Ala) caused the re-localization of BSK1 from the PM to the cytoplasm (26), indicating that *N*-myristoylation is critical for the PM association of BSK1. BSK1 also contains Cys residues potentially

Author affiliations: [a]Frontiers Science Center for Cell Responses, College of Life Sciences, Nankai University, Tianjin 300071, China; and [b]College of Life Sciences, Shandong Agricultural University, Tai'an 271018, China

Author contributions: S.L. and Y.Z. conceived and supervised the project; F.L. performed the experiments with the assistance of P.-Y.Q., J.-P.L., L.-N.Y., Y.-J.G., and J.-Y.L.; S.L., Y.Z., and F.L. designed the experiments and analyzed the data; S.L., Y.Z., and F.L. wrote the article with contributions from all the authors. All authors read and approved of the manuscript.

The authors declare no competing interest.

This article is a PNAS Direct Submission.

[1]To whom correspondence may be addressed. Email: shali@sdau.edu.cn or yzhang2020@nankai.edu.cn.

This article contains supporting information online at https://www.pnas.org/lookup/suppl/doi:10.1073/pnas.2322375121/-/DCSupplemental.

Published February 5, 2024.

subjected to *S*-acylation (SwissPalm, http://swisspalm.epfl.ch). Indeed, a recent study demonstrated that BSK1 is *S*-acylated (27). However, PATs catalyzing their *S*-acylation are unclear.

We report that three class C PATs regulate the *S*-acylation of BSK1 and play positive roles in BR signaling. *PAT19*, *PAT20*, and *PAT22* are constitutively expressed, and their protein products are associated with the PM and the *trans*-Golgi network/early endosomes (TGN/EE). Functional loss of *PAT19*, *PAT20*, and *PAT22* results in a pleiotropic phenotype resembling those of BR-defective mutants, showing dwarfism, small rosettes, reduced root length, reduced hypocotyl length, and increased stomatal density. By genetic approaches, we demonstrate that functional loss of *PAT19*, *PAT20*, and *PAT22* results in defective BR signaling. PAT19, PAT20, and PAT22 interact with BSK1 but not CDG1, indicating enzyme–substrate specificity. Indeed, *S*-acylation of BSK1 was substantially reduced in the triple mutants of *PAT19*, *PAT20*, and *PAT22*. We further show that the PM abundance of BSK1 is reduced in the triple mutants of *PAT19*, *PAT20*, and *PAT22* whereas abolished by its *S*-acylation-deficient point mutations, suggesting a key role of *S*-acylation in its PM targeting. Finally, brassinolide (BL) induces vacuolar trafficking and degradation of PAT19, PAT20, and PAT22, suggesting that the *S*-acylation of BSK1 by the three PATs serves as a negative feedback module in BR signaling.

Results

Three Functionally Unknown Class C PATs Are Targeted to the PM and TGN/EE. Arabidopsis PATs are separated into several subfamilies (6). PAT18, PAT19, PAT20, PAT21, and PAT22 belong to the class C group, among which PAT21 was recently reported to mediate gametophytic development (28) while function of the other four has not been characterized. Because PATs are transmembrane proteins, whose targets often are determined by their localization at distinct membrane compartments (4, 17), we first examined the subcellular localization of these PATs. We generated *UBQ10:PAT-GFP* transgenic plants expressing PAT-GFP fusions and examined GFP distributions by confocal laser scanning microscopy (CLSM) and by co-labeling with FM4-64, which is a lipophilic dye that first marks the plasma membrane (PM), then enters into endomembrane compartments via endocytosis. Among the four class C PATs, PAT19, PAT20, and PAT22 were distributed at the PM and cytosolic vesicles (Fig. 1 *A*–*C*) whereas PAT18 was not detected at the PM, only in cytosolic vesicles (*SI Appendix*, Fig. S1*A*). To determine the identity of these vesicles, we applied brefeldin A (BFA), a fungal toxin that caused the accumulation of internalized FM4-64 into cytosolic compartments, called BFA compartments that are aggregated *trans*-Golgi network/early endosomes (TGN/EE) at the core while surrounded by Golgi apparatus. In BFA-treated *UBQ10:PAT19-GFP*, *UBQ10:PAT20-GFP*, or *UBQ10:PAT22-GFP* roots, GFP signals showed a complete overlap with FM4-64 signals in the BFA compartments (Fig. 1 *D*–*F*), indicating that PAT19, PAT20, and PAT22 were associated with TGN/EE in addition to the PM. By contrast, BFA treatment caused PAT18-GFP signals to surround FM4-64-labeled BFA compartments (*SI Appendix*, Fig. S1*C*), indicating its Golgi distribution. To verify the Golgi distribution of PAT18-GFP, we crossed the *UBQ10:PAT18-GFP* transgenic plants with WAVE22R, a transgenic line expressing a RFP-fused Golgi marker (29). Indeed, PAT18-GFP co-localized with RFP-positive vesicles (*SI Appendix*, Fig. S1 *A* and *B*). The similar localization of PAT19, PAT20, and PAT22, but not PAT18, implies a redundant function of the three class C PATs.

***PAT19*, *PAT20*, and *PAT22* Are Constitutively Expressed.** Functional similarity of PATs is not only determined by their subcellular localization but also by their expression patterns. We next examined the expression patterns of *PAT19*, *PAT20*, and

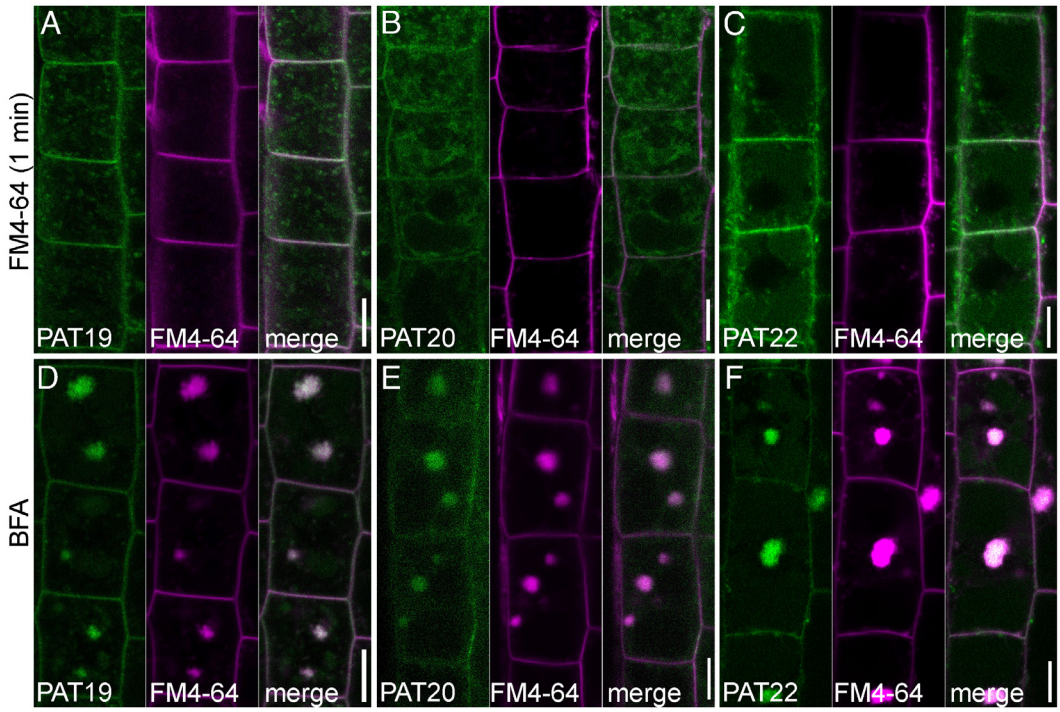

Fig. 1. Arabidopsis PAT19, PAT20, and PAT22 are targeted to the PM and TGN/EE. (*A*–*F*) Representative confocal laser scanning microscopy (CLSM) of root epidermal cells from *UBQ10:PAT19-GFP* (*A* and *D*), *UBQ10:PAT20-GFP* (*B* and *E*), and *UBQ10:PAT22-GFP* plants (*C* and *F*). Seedlings at 5 d after germination (DAG) were pulsed-labeled with FM4-64 (*A*–*C*) or treated with BFA for 50 min (*D*–*F*). Merges of the GFP and RFP (magenta, for FM4-64) channels are shown at the right side of corresponding images. (Bars, 10 μm.)

PAT22 by reverse transcription quantitative PCRs (RT-qPCRs) and by histochemical GUS staining of promoter:GUS reporter transgenic plants. Based on RT-qPCRs, all three genes showed similar expression patterns, i.e., constitutively expressed in all tissues with some variabilities (*SI Appendix*, Fig. S2 *S–U*). Based on histochemical GUS staining, we determined that *PAT19* (*SI Appendix*, Fig. S2 *A–F*), *PAT20* (*SI Appendix*, Fig. S2 *G–L*), and *PAT22* (*SI Appendix*, Fig. S2 *M–R*) were expressed in most tissues or cells, including leaves (*SI Appendix*, Fig. S2 *A*, *G*, and *M*), roots (*SI Appendix*, Fig. S2 *C*, *I*, and *O*), inflorescences (*SI Appendix*, Fig. S2 *F*, *L*, and *R*), hypocotyls (*SI Appendix*, Fig. S2 *B*, *H*, and *N*), ovules (*SI Appendix*, Fig. S2 *E*, *K*, and *Q*), and stomata lineage cells (*SI Appendix*, Fig. S2 *D*, *J*, and *P*). The constitutive and overlapping expression patterns indicate that the three class C PATs redundantly participate in multiple developmental processes.

Generation and Characterization of *PAT* Mutants. To functionally characterize the three class C PATs, which have the same subcellular distribution and similar expression patterns, we took a reverse genetic approach. We isolated T-DNA insertion lines of *PAT19*, *PAT20*, *PAT22*, and by RT-PCRs obtained their homozygous mutant *pat19-1*, *pat20-1*, and *pat22-1*, respectively (*SI Appendix*, Fig. S3*A*). None of the single mutants showed growth defects (*SI Appendix*, Fig. S3 *E–G*), as would be expected due to potential functional redundancy. We thus generated hierarchy mutants by crosses. Among the hierarchy mutants, three types of double mutants were comparable to the wild type in plant growth (*SI Appendix*, Fig. S3 *E–G*). Only the triple mutant, i.e., *pat19-1*;*pat20-1*;*pat22-1* showed growth defects, including dwarfism and small rosettes (*SI Appendix*, Fig. S3 *E–G*), and reduced root length (*SI Appendix*, Fig. S3*D*). Because *pat19-1* and *pat20-1* expressed partial transcripts of *PAT19* (*SI Appendix*, Fig. S3*B*) and *PAT20* (*SI Appendix*, Fig. S3*C*), respectively, we suspected that the *pat19-1*;*pat20-1*;*pat22-1* represented a weak mutant allele. Thus, we generated additional mutants by using CRISPR/Cas9 genomic editing. We obtained two different mutants from the progenies of T-DNA-free Cas9-edited plants (Fig. 2 *A–C*). The two mutants, *pat19-2*;*pat20-2*;*pat22-2* and *pat19-3*;*pat20-2*;*pat22-2*, indeed showed similar albeit stronger growth defects (Fig. 2 *D* and *E*) than those of *pat19-1*;*pat20-1*;*pat22-1* (*SI Appendix*, Fig. S3 *E–G*). Introducing a genomic PAT20-GFP translational fusion construct (*PAT20g:GFP*) into either *pat19-2*;*pat20-2*;*pat22-2* or *pat19-3*;*pat20-2*;*pat22-2* fully rescued their growth defects (Fig. 2 *F* and *G* and *SI Appendix*, Fig. S4), confirming the identity of the triple mutants.

Functional Loss of *PAT19*, *PAT20*, and *PAT22* Compromises BR Signaling. Phenotypes of the *PAT* triple mutants greatly resembled those of BR deficient mutants, such as dwarfism, smaller rosettes, and reduced root length (22, 26, 30–32). We thus suspected that BR signaling was compromised in the *PAT* triple mutants. To gain a better idea, we examined BR-related developmental processes in the *PAT* triple mutants in detail. Specifically, the development of root apical meristem (RAM) (30, 31), stomatal development (33, 34), hypocotyl elongation (35), as well as ovule development (36, 37) are developmental processes in which BR signaling plays a major role.

Compared to wild type (Fig. 3 *A* and *D*), the *PAT* triple mutants showed a reduced RAM length (Fig. 3 *B*, *C*, and *H*) with disorganized quiescent centers (QC) (Fig. 3 *E* and *F*). Hypocotyl elongation in darkness was significantly reduced in the *PAT* triple mutants compared to that in wild type (Fig. 3 *G* and *I* and *SI Appendix*, Fig. S5). BR deficiency results in more guard cells (33, 34). Consistently, stomatal density was significantly increased in the *PAT* triple mutants (Fig. 3 *J*, *L*, and *M*) compared to that in wild type (Fig. 3 *J* and *K* and *SI Appendix*, Fig. S5). In addition, similar to BR deficient mutants in which ovule number per pistil was reduced (36) and integument growth was defective (37), the *PAT* triple mutants showed a significantly reduced ovule number per pistil and defective integument growth (*SI Appendix*, Fig. S6). Introducing *PAT20g:GFP* into the *PAT* triple mutants fully complemented their reduced RAM length (Fig. 3*H*), stomatal development (Fig. 3*J*), reduced hypocotyl elongation (Fig. 3*I*), and ovule developmental defects (*SI Appendix*, Fig. S6). These results support that functional loss of *PAT19*, *PAT20*, and *PAT22* results in reduced BR signaling.

To test whether the *PAT* triple mutants were compromised in BR signaling, we took pharmacological, molecular, and genetic approaches. We first examined the effect of brassinolide (BL), the active BR analog (22), on hypocotyl elongation and root growth. BL at 100 nM significantly reduced dark-induced hypocotyl elongation in the wild type (Fig. 4 *A*, *B*, and *E*), as reported (22, 38). In comparison, hypocotyl elongation in the *PAT* triple mutants was less sensitive to BL (Fig. 4 *A*, *B*, and *E*). Similarly, BL caused a significant higher reduction in root length of the wild type (22) than that in the *PAT* triple mutants (Fig. 4 *C*, *D*, and *F*). The

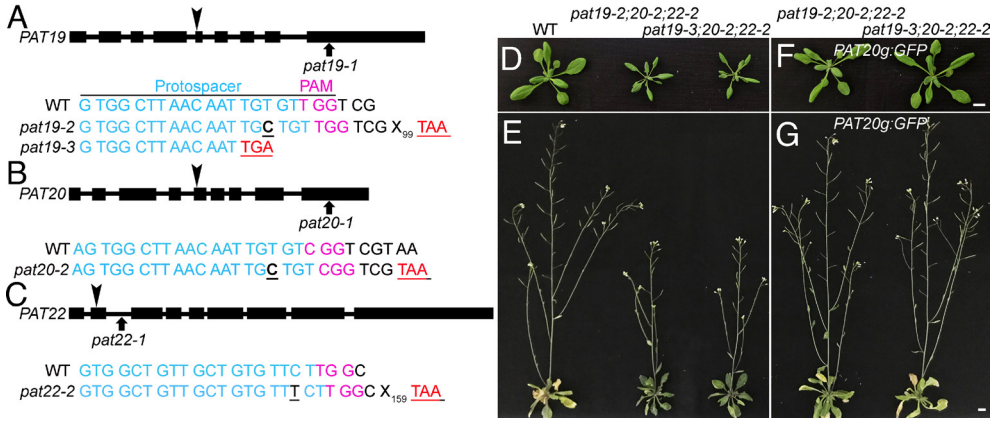

Fig. 2. *PAT19*, *PAT20*, and *PAT22* redundantly mediate plant growth. (*A–C*) Genomic structure and CRISPR/Cas9-based editing of *PAT19* (*A*), *PAT20* (*B*), or *PAT22* (*C*). The T-DNA insertion sites are indicated by arrows while the CRISPR/Cas9-target sites are indicated by arrowheads on the corresponding genomic loci. For Cas9-targets, PAM sequences and protospacer sequences are indicated by magenta and blue letters, respectively. Cas9-generated base pair insertion is in bold black within the protospacer sequences, which introduced pre-stop codons (red and underlined). (*D* and *E*) Representative wild type, *pat19-2;pat20-2;pat22-2* (*triplepat-2*), and *pat19-3;pat20-2;pat22-2* (*triplepat-3*) plants at 3 WAG (*D*) or 6 WAG (*E*). (*F* and *G*) Representative *PAT20g:GFP;pat19-2;pat20-2;pat22-2* (Comp;2), or *PAT20g:GFP;pat19-3;pat20-2;pat22-2* (Comp;3) plants at 3 WAG (*F*) or 6 WAG (*G*). [Bars, 1 cm for (*D* and *F*); 5 cm for (*E* and *G*).]

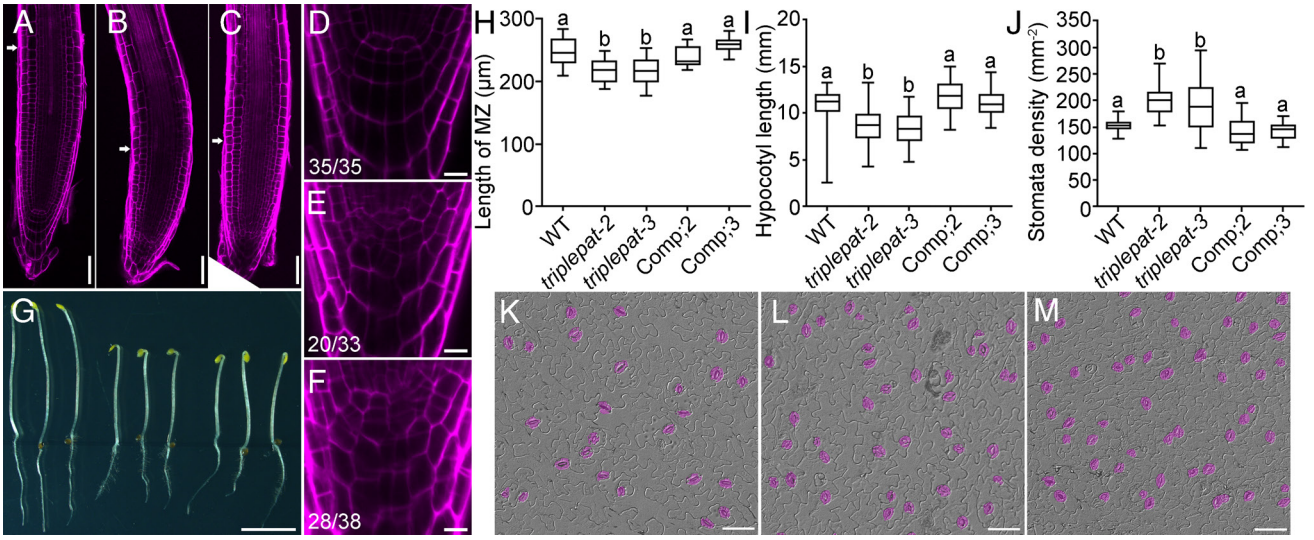

Fig. 3. The triple mutants of *PAT19*, *PAT20*, and *PAT22* show phenotypes indicative of reduced BR signaling. (*A*–*C*) Representative CLSM images of PI-stained roots from wild type (*A*), *pat19-2;pat20-2;pat22-2* (*triplepat-2*, *B*), and *pat19-3;pat20-2;pat22-2* (*triplepat-3*, *C*). The length of root apical meristem (RAM) is indicated from the site of an arrow to the corresponding root tip. (*D*–*F*) Representative CLSM images of the QC from PI-stained 5 DAG wild type (*D*), *pat19-2;pat20-2;pat22-2* (*E*), and *pat19-3;pat20-2;pat22-2* (*F*) roots. Numbers at the bottom indicate displayed/total examined. (*G*) A representative hypocotyl elongation experiment with designated genotypes. (*H*–*J*) Quantification of RAM length (*H*), hypocotyl length (*I*), and stomata density (*J*). Results shown are means ± SD ($n > 20$). Different letters indicate significantly different groups (one-way ANOVA, Tukey's multiple comparisons test, $P < 0.05$). (*K*–*M*) Differential interference contrast (DIC) images of leaf epidermal peels from wild type (*K*), *pat19-2;pat20-2;pat22-2* (*L*), and *pat19-3;pat20-2;pat22-2* (*M*) showing the distribution of stomata (highlighted in pink). [Bars, 50 μm for (*A*–*C*, *K*–*M*); 10 μm for (*D*–*F*); 5 mm for (*G*).]

BL-hyposensitivity of the *PAT* triple mutants suggested a reduced BR signaling. We also examined the expression of marker genes in BR signaling or BR biosynthesis. The induction of *SMALL AUXIN UP RNA 1* (*SAUR-AC1)* in the wild type by BL was abolished in the *PAT* triple mutants (Fig. 4*G*), whereas the reduction of *DWARF4 (DWF4)* in the wild type by BL treatment was not significantly changed in the *PAT* triple mutants (Fig. 4*H*). These results support a positive role of *PAT19*, *PAT20*, and *PAT22* in BR signaling.

To further demonstrate that the *PAT* triple mutants were compromised in BR signaling, we took a genetic approach by overexpressing *BZR1* in *pat19-2;pat20-2;pat22-2*. Overexpressing BZR1-GFP in *pat19-2;pat20-2;pat22-2* rescued its reduced root growth (Fig. 5 *A* and *C*–*E*) and hypocotyl elongation (Fig. 5 *B* and *F*), demonstrating

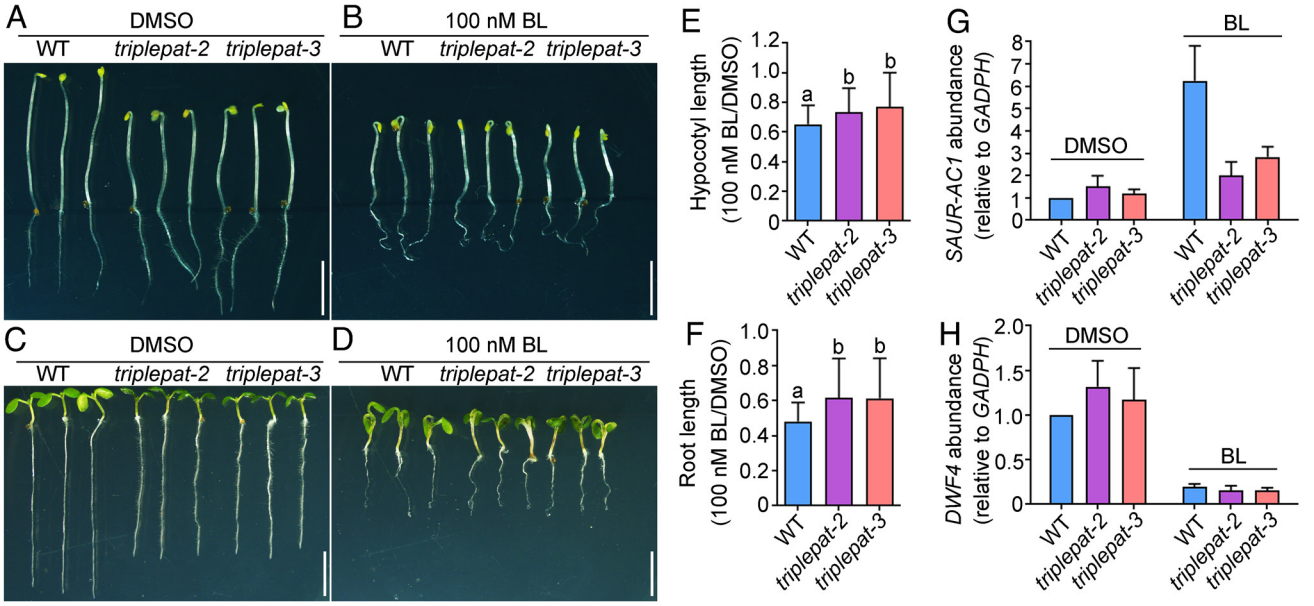

Fig. 4. Functional loss of *PAT19*, *PAT20*, and *PAT22* results in hyposensitivity to BL. (*A*–*D*) A representative hypocotyl elongation experiment (*A* and *B*) and root growth assay (*C* and *D*). For simplicity, *triplepat-2* indicates *pat19-2;pat20-2;pat22-2* and *triplepat-3* indicates *pat19-3;pat20-2;pat22-2*. (*E*) Quantification of hypocotyl length showing the effect of 100 nM BL treatment (*B*) versus DMSO (*A*). Sterilized seeds were grown on 1/2 MS plates supplemented with DMSO or 100 nM BL for 5 d under dark before measurement. (*F*) Quantification of root growth showing the effect of 100 nM BL treatment (*D*) versus DMSO (*C*). Sterilized seeds were grown on 1/2 MS plates supplemented with DMSO or 100 nM BL for 7 d before measurement. For (*E* and *F*), results shown are means ± SD ($n = 70$). Different letters indicate significantly different groups (one-way ANOVA, Tukey's multiple comparisons test, $P < 0.05$). (*G* and *H*) Reverse transcription quantitative PCRs (RT-qPCRs) of *SAUR-AC1* (*G*) or *DWF4* (*H*) abundance in wild type versus in *triplepat* mutants upon DMSO treatment or 100 nM BL treatment. Expression levels are related to that of *GADPH*. Seedlings at 7 DAG were incubated in liquid MS medium supplemented with either DMSO or 100 nM BL for 2 h before RNA extractions. Results shown are means ± SEM ($n = 3$). Each biological replicates were repeated three times with similar results. (Bar, 5 mm.)

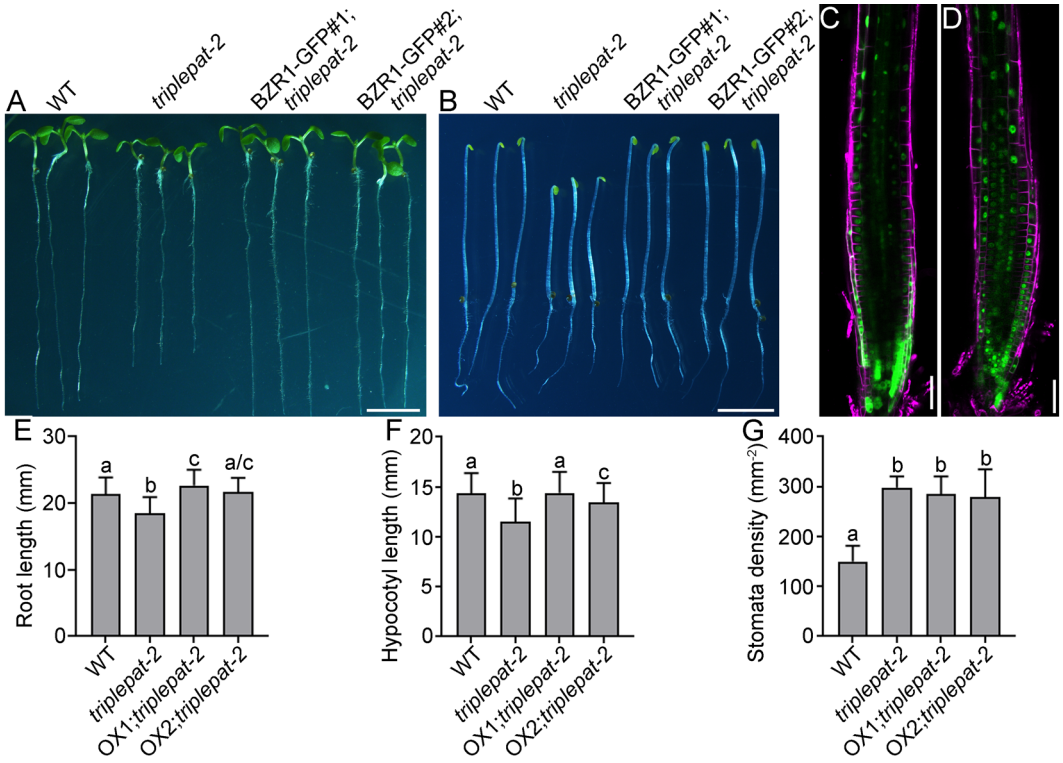

Fig. 5. Overexpression of BZR1-GFP rescues hypocotyl elongation and root growth but not stomatal development of the *pat19-2;pat20-2;pat22-2* triple mutant. (*A* and *B*) A representative root growth (*A*) or hypocotyl elongation assay (*B*) with designated genotypes. For simplicity, *triplepat-2* indicates *pat19-2;pat20-2;pat22-2*. (*C* and *D*) A representative CLSM of a primary root from two independent lines of *BZR1-GFP;pat19-2;pat20-2;pat22-2* (*C* and *D*). FM4-64 (magenta) was used to label cell membrane. (*E*–*G*) Quantification of primary root length at 1 WAG (*E*), hypocotyl length (*F*), or stomata density (*G*). Results shown are means ± SD ($n > 30$). Different letters indicate significantly different groups (one-way ANOVA, Tukey's multiple comparisons test, $P < 0.01$). [Bars, 5 mm for (*A* and *B*); 50 μm for (*C* and *D*).]

that defects in *pat19-2;pat20-2;pat22-2* were due to reduced BR signaling. Overexpressing BZR1-GFP in *pat19-2;pat20-2;pat22-2* did not suppress its ectopic stomatal development (Fig. 5*G*), which is consistent with the fact that BR regulates stomatal development in a BZR1-independent manner (34).

PAT19, PAT20, and PAT22 Physically and Genetically Interact with BSK1. As the major class of protein *S*-acyl transferases, PATs presumably function through substrate *S*-acylation. To test whether the three PATs mediated BR signaling through their enzymatic activity, we generated a PAT20 variant, $PAT20^{C202S}$, in which the Cys residue within its catalytic motif was mutated to Ser, and thus potentially abolishing its PAT activity as reported for other PATs (4, 10). Introducing $PAT20^{C202S}$-GFP into the *PAT* triple mutants did not complement their phenotypes, including reduced root growth, reduced hypocotyl elongation, dwarfism, and smaller rosettes (*SI Appendix*, Fig. S7). These results suggest that PAT19, PAT20, and PAT22 mediate BR signaling by *S*-acylation of substrate proteins.

Both BSK1 and CDG1 are positive regulators of BR signaling and associated with the PM (23). CDG1 (23) and recently BSK1 (27) have been shown to be *S*-acylated. We thus hypothesized that PAT19, PAT20, and PAT22 catalyzed the *S*-acylation of BSK1 or CDG1 to play a positive role in BR signaling. To test this hypothesis, we first examined whether PAT19, PAT20, and PAT22 interacted with BSK1 or CDG1. By mating-based split-ubiquitin (mbSUS) yeast two hybrid (Y2H) and by split luciferase (SplitLUC) assays, we determined that PAT19, PAT20, and PAT22 interacted with BSK1 but not CDG1 (*SI Appendix*, Fig. S8). In addition, in vitro pull-down assays demonstrated that BSK1 interacted with the DHHC domain of PAT19, PAT20, and PAT22 (*SI Appendix*, Fig. S8). These results suggested that BSK1 but not CDG1 was likely a substrate of TRIPLEPAT.

***S*-acylation of BSK1 Is Substantially Reduced in the *PAT* Triple Mutant and Abolished by CC3/4SS Mutations.** We next examined whether BSK1 was *S*-acylated. The same *UBQ10:BSK1-GFP* transgene was examined in the wild type or in *pat19-2;pat20-2;pat22-2* by crosses for comparison. By using the *S*-acylated Calcineurin B-like3 (CBL3) as the positive control (17), we demonstrated that BSK1 was *S*-acylated and its *S*-acylation was substantially reduced in *pat19-2;pat20-2;pat22-2* (Fig. 6*A*), suggesting that the PAT19, PAT20, and PAT22 were critical for the *S*-acylation of BSK1. Two Cys residues within the N terminus of BSK1 close to the N-myristoylated Gly, Cys^3, and Cys^4, were predicted to be *S*-acylation sites (CSS-Palm). It was recently shown that a C3S mutation in BSK1 caused a substantial reduction of *S*-acylation and of BSK1 membrane anchoring (27). We thus generated $BSK1^{CC3/4SS}$, in which both of the Cys residues were mutated to Ser residues. Indeed, *S*-acylation of BSK1 was abolished by the CC3/4SS mutations (Fig. 6*B*).

To further explore the role of *S*-acylation and the three *PATs* in the function of BSK1, we examined the interaction between BSK1-GFP and BRI1-mCherry by Förster resonance energy transfer (FRET) assays. Indeed, the interaction between BSK1-GFP and BRI1-mCherry was significantly reduced in *pat19-2;pat20-2;pat22-2* compared to that in wild type (Fig. 6*C* and *SI Appendix*, Fig. S9). To verify that the effect of *PAT* loss-of-function on BSK1–BRI1 interaction was specific, we also examined the interaction between BSK1 and BRI1 in a *PAT* mutant, in which five Arabidopsis class A PATs, i.e., *PAT1*, *PAT2*, *PAT3*, *PAT4*, and *PAT8*, were mutated (Xiang et al., accompany manuscript). Indeed,

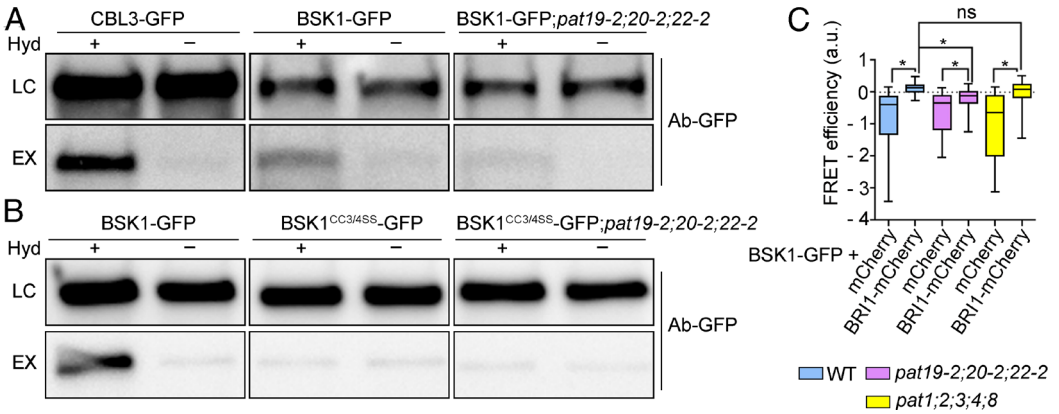

Fig. 6. The *S*-acylation of BSK1 is reduced by functional loss of *PAT19*, *PAT20*, and *PAT22* or by the CC3/4SS mutations. (*A* and *B*) The *S*-acylation state of BSK1 is reduced in *pat19-2;pat20-2;pat22-2* (*A*) or by CC3/4SS mutation (*B*) using the acyl-RAC assay. LC: loading control; EX: experimental (*S*-acylation state); Hyd^+, hydroxylamine present (selectively cleaves *S*-acyl groups); Hyd^-, hydroxylamine absent (*S*-acyl groups not cleaved). Proteins are considered to be *S*-acylated if a signal is observed in the Hyd^+ lane and not in the Hyd^- lane for the EX samples. The *S*-acylated protein CBL3 was used as the internal control. (*C*) FRET efficiency demonstrating that the interaction between BSK1-GFP and BRI1-mCherry depends on *PAT19*, *PAT20*, and *PAT22*. The combination of BSK1-GFP and mCherry was used as a negative control. Results are means ± SD ($n > 30$). Each combination was examined with three replicate experiments. Asterisks indicate significant difference (*t*-test, $P < 0.0001$). a.u. stands for arbitrary fluorescence unit.

the interaction between BSK1 and BRI1 was not affected by functional loss of *PAT1*, *PAT2*, *PAT3*, *PAT4*, and *PAT8* (Fig. 6*C* and *SI Appendix*, Fig. S9). These results demonstrated the importance of *PAT19, PAT20*, and *PAT22* for the role of BSK1 in BR signaling.

To provide further evidence supporting that BSK1 was *S*-acylated at Cys^3 and Cys^4 residues, and its *S*-acylation was critical for BR signaling, we overexpressed BSK1-GFP (Fig. 7 *F* and *G*) or $BSK1^{CC3/4SS}$-GFP (Fig. 7 *H* and *I*) in *pat19-2;pat20-2;pat22-2*. Over-expression of BSK1-GFP fully rescued the reduced root growth and hypocotyl elongation (Fig. 7 *A–D*) whereas partially suppressed ectopic stomatal development in *pat19-2;pat20-2;pat22-2* (Fig. 7*E*). By contrast, overexpressing $BSK1^{CC3/4SS}$-GFP did not rescue the reduced root growth (Fig. 7 *A* and *C*) or hypocotyl elongation (Fig. 7 *B* and *D*) in *pat19-2;pat20-2;pat22-2*. Nor did overexpressing $BSK1^{CC3/4SS}$-GFP suppress the ectopic stomatal development in *pat19-2;pat20-2;pat22-2* (Fig. 7*E*). These results suggest that *S*-acylation of BSK1 at Cys^3 and Cys^4 residues is critical for its function.

The Three Class C PATs and *S*-acylation Mediate the PM Targeting of BSK1. Because protein *S*-acylation often affects the subcellular targeting of substrate proteins (5, 25), we examined whether the subcellular localization of BSK1 was affected by its *S*-acylation. By examining the same *UBQ10:BSK1-GFP* transgenes in wild type versus in *pat19-2;pat20-2;pat22-2* (Fig. 7 *F* and *G*), we determined that BSK1-GFP was distributed at the PM both

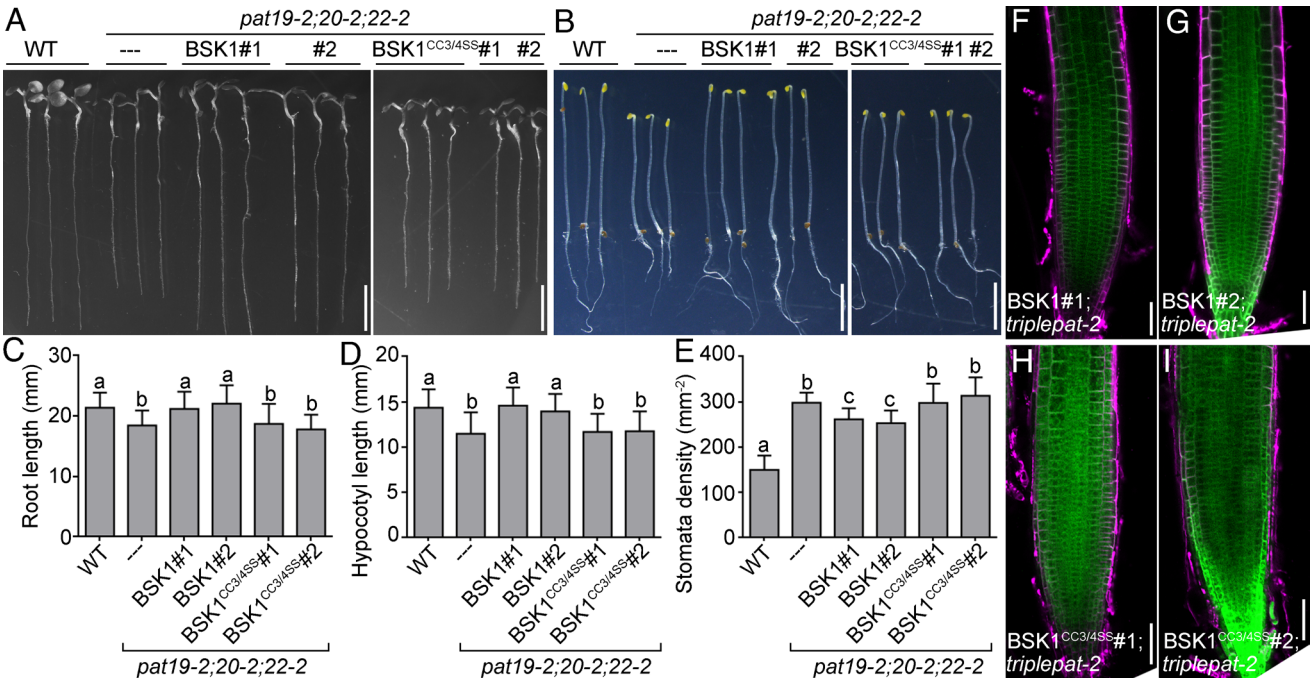

Fig. 7. Over-expression of BSK1 but not $BSK1^{CC3/4SS}$ rescues the phenotypes of the *pat19-2;pat20-2;pat22-2* triple mutant. (*A* and *B*) A representative root growth (*A*) or hypocotyl elongation assay (*B*) with designated genotypes. (*C–E*) Quantification of primary root length at 1 WAG (*C*), hypocotyl length (*D*), or stomata density (*E*). Results shown are means ± SD ($n > 30$). Different letters indicate significantly different groups (one-way ANOVA, Tukey's multiple comparisons test, $P < 0.01$). (*F–I*) A representative CLSM of a primary root from two lines of *BSK1-GFP;pat19-2;pat20-2;pat22-2* (*F* and *G*) or two lines of $BSK1^{CC3/4SS}$-GFP;*pat19-2;pat20-2;pat22-2* (*H* and *I*). FM4-64 (magenta) was used to label cell membrane. [Bars, 5 mm for (*A* and *B*); 50 μm for (*F–I*).]

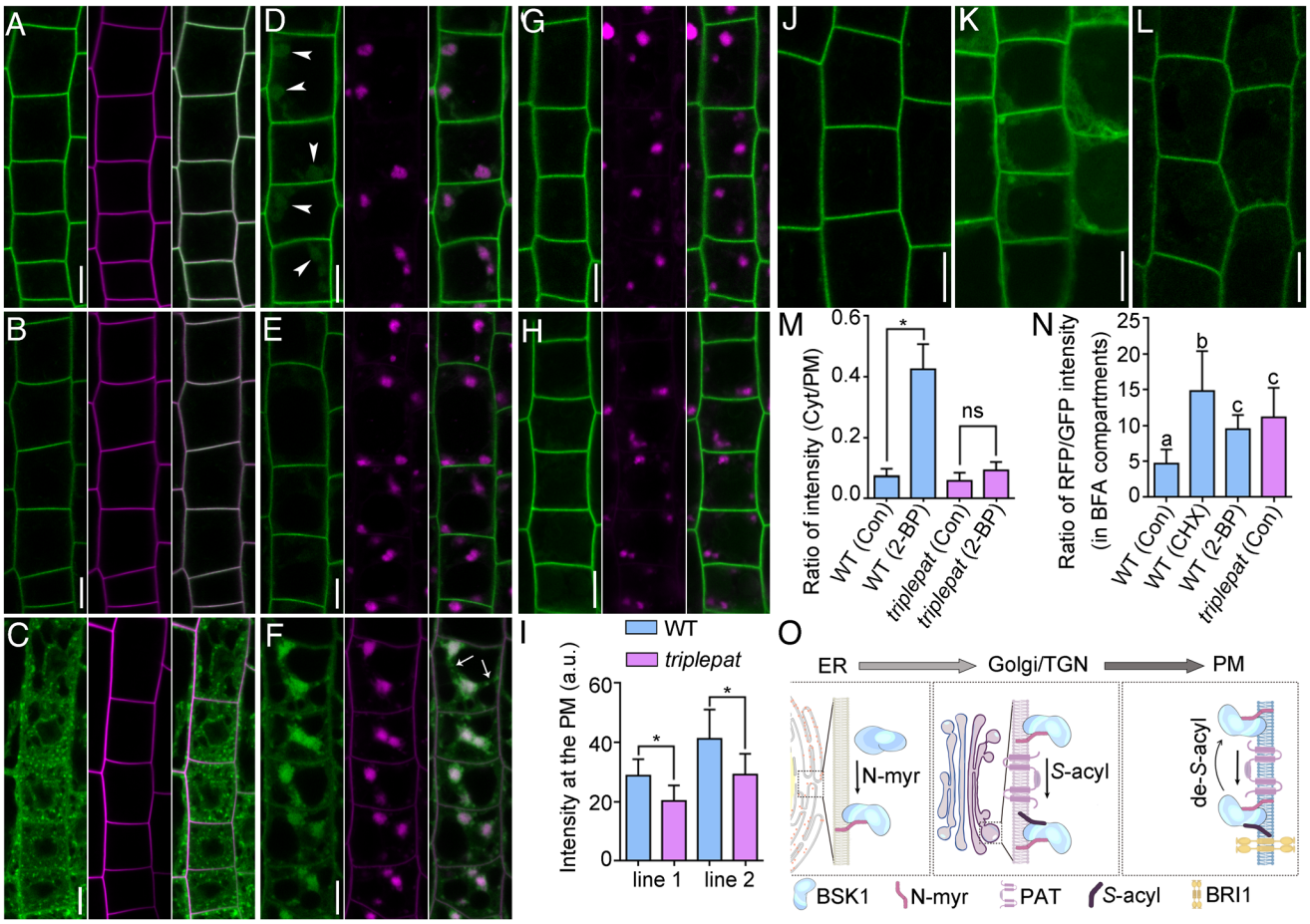

Fig. 8. Subcellular localization of BSK1 is influenced by functional loss of *PAT19*, *PAT20*, and *PAT22* or by the CC3/4SS mutations. (*A–C*) CLSM of root cells from *BSK1-GFP* (*A*), *BSK1-GFP;pat19-2;pat20-2;pat22-2* (*B*), or *BSK1*$^{CC3/4SS}$*-GFP* (*C*). Seedlings were pulse-labeled with FM4-64. (*D–F*) CLSM of root cells from *BSK1-GFP* (*D*), *BSK1-GFP;pat19-2;pat20-2;pat22-2* (*E*), or *BSK1*$^{CC3/4SS}$*-GFP* (*F*). Seedlings were pulse-labeled with 4 μM FM4-64 and treated with 50 μM BFA for 50 min before imaging. Arrowheads point at BFA compartments accumulating BSK1-GFP; arrows point at *trans*-vacuolar strands in one cell of (*F*). (*G* and *H*) CLSM of root cells from *BSK1-GFP* incubated with CHX (*G*) or with 20 μM 2-BP (*H*) for 12 h and then treated with 50 μM BFA for 50 min before imaging. For (*A–H*), from left to right are the GFP channel, the RFP channel, merge of the GFP and RFP channel images. (*I*) Quantification of BSK1-GFP intensity at the PM. Results are means ± SD ($n = 20$); a.u., arbitrary fluorescence unit; asterisks indicate significant difference (*t*-test, $P < 0.05$). (*J–L*) CLSM of root cells from *BSK1-GFP* (*J* and *K*) or *BSK1-GFP;pat19-2;pat20-2;pat22-2* (*L*) treated with DMSO (*J*) or 20 μM 2-BP (*K* and *L*) for 12 h before imaging. (*M*) Ratio of BSK1-GFP signals between cytoplasm and the PM. Results are means ± SD ($n = 20$); the asterisk indicates significant difference (*t*-test, $P < 0.01$); ns, no significant difference (*t*-test, $P > 0.05$). (*N*) Ratio of FM4-64 signals versus BSK1-GFP signals within BFA compartments. Results are means ± SD ($n = 20$). Different letters indicate significantly different groups (one-way ANOVA, Tukey's multiple comparisons test, $P < 0.01$). (*O*) A working model. *N*-myristoylation allows the insertion of BSK1 to the ER; BSK1 is transported to the Golgi/TGN by anterograde trafficking where it is *S*-acylated by PAT19, PAT20, and PAT22; N-myristoylated and double *S*-acylated BSK1 is targeted to the PM for BRI1 interaction while PAT19, PAT20, and PAT22 at the PM prevents de-*S*-acylation of BSK1. (Bars, 10 μm.)

in wild type (Fig. 8*A*) and in *pat19-2;pat20-2;pat22-2* (Fig. 8*B*), although its abundance at the PM was significantly reduced in *pat19-2;pat20-2;pat22-2* (Fig. 8*I*). Because two *UBQ10:BSK1-GFP* transgenes were comparable (Fig. 8*A*), we demonstrated data using *UBQ10:BSK1-GFP#1* for simplicity.

There was a substantial portion of PAT19, PAT20, and PAT22 associated with the TGN/EE in addition to the PM (Fig. 1). Therefore, we examined whether BSK1-GFP was delivered to the PM via the TGN/EE by applying BFA. Most GFP signals were colocalized with FM4-64-positive BFA compartments indicative of the TGN/EE identity whereas a portion of GFP signals were distributed at Golgi/endoplasmic reticulum (ER) in the wild type upon BFA treatment (Fig. 8*D*). Pre-treatment with cycloheximide (CHX), an inhibitor for protein de novo biosynthesis, significantly reduced BFA compartment-associated BSK1-GFP signals (Fig. 8 *G* and *N*), indicating that BFA compartment-associated BSK1-GFP was mostly newly synthesized proteins, consistent with a previous report that BSK1 was not dynamically recycled at the PM (21). In comparison, BFA treatment of BSK1-GFP;*pat19-2;pat20-2;pat22-2* or of BSK1-GFP pre-incubated with 2-bromopalmitate (2-BP), an inhibitor of *S*-acylation (39), resulted in a substantial reduction of BFA compartment-associated BSK1-GFP (Fig. 8 *E*, *H*, and *N*), similar to BSK1-GFP treated with BFA and CHX (Fig. 8*G*). The BFA insensitivity of BSK1-GFP in *pat19-2;pat20-2;pat22-2* or by pre-treatment of 2-BP indicates that the three class C PATs and *S*-acylation participate in the trafficking of newly synthesized BSK1 on route to the PM (Fig. 8*O*). Indeed, 2-BP treatment resulted in reduced PM abundance of BSK1-GFP compared to DMSO treatment (Fig. 8 *J*, *K*, and *M*), as reported recently (27). 2-BP treatment did not cause a reduced PM abundance of BSK1-GFP in *pat19-2;pat20-2;pat22-2* (Fig. 8 *L* and *M*), indicating that 2-BP inhibited the activity of the three class C PATs toward BSK1-GFP in wild type

Surprisingly, BSK1$^{CC3/4SS}$-GFP lost its PM association completely and was distributed to cytosolic vesicles (Fig. 8*C*). BFA treatment caused the accumulation of BSK1$^{CC3/4SS}$-GFP into FM4-64-positive BFA compartments, with a small portion of BSK1$^{CC3/4SS}$-GFP at transvacuolar strands and surface of BFA compartments (Fig. 8*F*), indicative of the TGN/EE and Golgi/ER identity. Because the Cys3 residue of BSK1 was reported to be the

major site of *S*-acylation (27), we also examined the distribution of BSK1^{C3S}-GFP (27) in detail. Similar to BSK1$^{CC3/4SS}$-GFP, BSK1^{C3S}-GFP signals were associated with cytosolic vesicles (*SI Appendix*, Fig. S10). Nevertheless, BSK1^{C3S}-GFP was also detected at the PM (*SI Appendix*, Fig. S10) where BSK1$^{CC3/4SS}$-GFP was absent (Fig. 8*C*). BFA treatment resulted in the accumulation of BSK1^{C3S}-GFP into FM4-64-positive BFA compartments, as well as Golgi/ER structures (*SI Appendix*, Fig. S10). These results further supported that double *S*-acylation at Cys3 and Cys4 is essential for the PM targeting of BSK1.

BL Induces Vacuolar Trafficking and Degradation of PAT19, PAT20, and PAT22. As to other phytohormones, BR negatively regulates some of its positive regulators and biosynthetic genes, either transcriptionally or post-translationally to keep its signaling in check (35). To determine whether *PAT19*, *PAT20*, and *PAT22* were transcriptionally responsive to BR, we applied BL and examined the expression of *PAT19*, *PAT20*, and *PAT22*. BL treatment induced the expression of *EXPANSIN A8* (*EXPA8*) (*SI Appendix*, Fig. S11) as reported (40). However, *PAT19*, *PAT20*, and *PAT22* were not transcriptionally affected by BL (*SI Appendix*, Fig. S11).

To determine whether PAT19, PAT20, and PAT22 were post-translationally affected by BR, we applied BL to seedlings of *UBQ10:PAT19-GFP*, *UBQ10:PAT20-GFP*, and *UBQ10:PAT22-GFP* transgenic plants with DMSO treatment as controls. For the control treatment, PAT19-GFP, PAT20-GFP, and PAT22-GFP were associated with the PM and vesicles (Fig. 9*A* and *SI Appendix*, Fig. S12), similar to that without any treatment (Fig. 1). By contrast, cells treated with BL showed GFP signals in vacuoles in addition to the PM (Fig. 9*B* and *SI Appendix*, Fig. S12), indicating that BL induced vacuolar trafficking of PAT19-GFP, PAT20-GFP, and PAT22-GFP. To verify this result, we applied BL together with Concanamycin A (ConcA) that inhibits the fusion between prevacuolar compartments/multivesicular compartments (PVC/MVB) with the tonoplast (41, 42). Treatment of ConcA together with BL resulted in a substantial portion of GFP signals in vesicular structures outside of vacuoles (Fig. 9*C* and *SI Appendix*, Fig. S12). We also applied E-64d, an inhibitor of papain family protease that inhibits vacuolar degradation of proteins (43). Treatment of E-64d together with BL resulted in a substantial increase of GFP signals inside vacuoles (Fig. 9*D* and *SI Appendix*, Fig. S12).

To exclude the possibility that BL treatment induced vacuolar trafficking in general, we performed similar treatments on seedlings expressing PAT4-GFP, which is another Arabidopsis PAT associated with both the PM and the TGN/EE (10). In contrast to PAT19-GFP, PAT20-GFP, and PAT22-GFP, the subcellular localization of PAT4-GFP was not affected by BL treatment (Fig. 9 *E*–*H*), i.e., BL did not induce vacuolar delivery of PAT4-GFP. These results confirmed that BR signaling specifically promoted vacuolar degradation of PAT19-GFP, PAT20-GFP, and PAT22-GFP.

Discussion

Functional loss of *PAT19*, *PAT20*, and *PAT22* results in a pleiotropic phenotype, including dwarfism, a reduction in root growth and RAM (Fig. 3 and *SI Appendix*, Figs. S3 and S4), a reduction in hypocotyl elongation (Fig. 3 and *SI Appendix*, Fig. S5), ectopic stomatal development (Fig. 3 and *SI Appendix*, Fig. S5), as well as a reduced number of ovules per pistil and defective integument growth (*SI Appendix*, Fig. S6). All of these have been associated with a compromised BR signaling (22, 32, 36, 37, 44–46), suggesting that *PAT19*, *PAT20*, and *PAT22* positively mediate BR signaling. Indeed, enhancing BR signaling by overexpressing *BZR1* fully rescues the defects of the *PAT* triple mutants, except for ectopic guard cells (Fig. 5), which is expected since BR-mediated stomatal development does not depend on BZR1 (33, 34).

Several lines of evidence suggest that PAT19, PAT20, and PAT22 catalyze the *S*-acylation of BSK1 to influence BR signaling. First, the expression of PAT20 (Figs. 2 and 3) but not that of PAT20^{C202S} (*SI Appendix*, Fig. S7), its potentially inactive variant, rescues the phenotype of the *PAT* triple mutants, indicating that PAT19, PAT20, and PAT22 mediate these developmental processes through substrate *S*-acylation. Second, PAT19, PAT20, and PAT22 interact with BSK1 through their catalytic domains whereas do not interact with CDG1 (*SI Appendix*, Fig. S8), hinting at enzyme–substrate specificity. Third, as reported recently (27), BSK1 is *S*-acylated and its *S*-acylation of BSK1 is substantially reduced in the *PAT* triple mutants (Fig. 6). Finally, overexpressing *BSK1* fully rescues root growth and hypocotyl elongation, and partially rescued

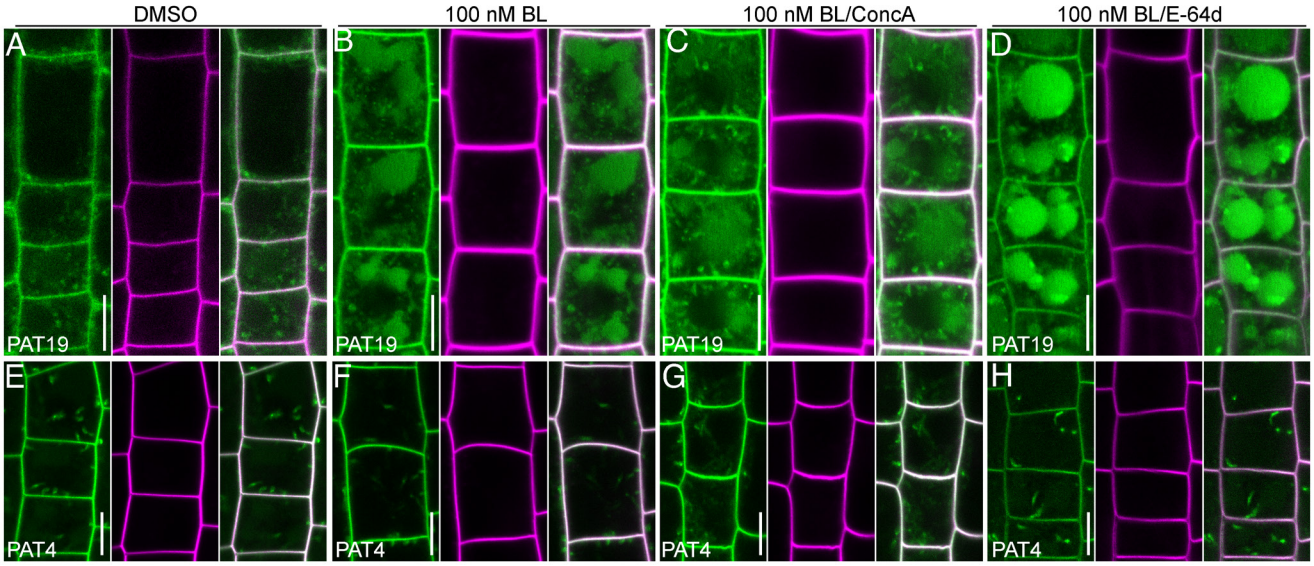

Fig. 9. BL induces vacuolar trafficking and degradation of PAT19. (*A*–*H*) CLSM of FM4-64 pulse-labeled root cells from *UBQ10:PAT19-GFP* seedlings (*A*–*D*) or *PAT4g:GFP;pat4* seedlings (*E*–*H*) at 4 DAG. Seedlings were treated with DMSO (*A* and *E*), with 100 nM BL (*B* and *F*), with 100 nM BL and 2 μM ConcA (*C* and *G*), or with 100 nM BL and 10 μM E-64d (*D* and *H*) before imaging. From left to right: the GFP channel, the RFP channel, merge of the GFP and RFP channels. (Bars, 10 μm.)

stomatal density in the *PAT* triple mutants (Fig. 7), supporting their genetic interaction. Although BSK1 explains most, if not all, phenotypic defects in the *PAT* triple mutants, we do not exclude the possibility that other proteins are *S*-acylated by PAT19, PAT20, or PAT22 since there are much more S-acylated proteins in the Arabidopsis than PATs.

The PAT-dependent *S*-acylation of BSK1 is critical for its interaction with BRI1 (Fig. 6 and *SI Appendix*, Fig. S9), which is essential for its role in BR signaling (22). It is interesting that BR negatively mediates the abundance of both BRI1 (42, 47) and these PATs (Fig. 9 and *SI Appendix*, Fig. S12) through vacuolar trafficking and degradation. PAT and S-acylation-dependent interaction between BSK1 and BRI1 initiate BR signaling to downregulate BRI1 and these PATs, indicating that the S-acylation of BSK1 by these PATs serves as a negative feedback module to keep BR signaling in check. Interestingly, a recent study (15) indicated that PAT5 and PAT9 were phosphorylated by their S-acylation substrates and it provides an additional layer of regulation, similar to the BL-induced vacuolar degradation of PAT19, PAT20, and PAT22. Considering that BSK1 is a functional kinase and most eukaryotic proteins contain potential phosphorylation sites, the possibility that the three class C PATs are phosphorylated by BSK1 is thus an interesting scenario worthy of future investigation.

We demonstrate that PAT-dependent *S*-acylation of BSK1 plays a key role in its targeting to the PM. BSK1-GFP is associated with the PM (Fig. 8). Upon BFA treatment, a portion of BSK1-GFP is distributed to BFA compartments, i.e., TGN/EE (Fig. 8). This TGN/EE-associated BSK1-GFP is from newly synthesized proteins since inhibiting protein synthesis by using CHX significantly reduced such distribution (Fig. 8). The result is consistent with a previous report demonstrating that BSK1 undergoes little if any endocytosis (21). Interestingly, in the *PAT* triple mutants or inhibiting *S*-acylation by 2-BP results in a significantly reduced accumulation of BSK1-GFP in BFA compartments, similar to the combined treatment of BFA and CHX in wild type (Fig. 8), suggesting that *PATs* and *S*-acylation are important for the targeting of newly synthesized BSK1 to the PM. Indeed, BSK1$^{CC3/4SS}$-GFP is associated with the TGN/EE but not the PM (Fig. 8), further supporting a critical role of *S*-acylation in BSK1 targeting from the TGN/EE to the PM.

It is intriguing that mutating the *S*-acylation sites of the tonoplast-associated CBLs results in their distribution to cytosol (3, 4, 17) whereas mutating those of BSK1 results in its localization to the TGN/EE (Fig. 8), despite that neither contains transmembrane domains. The difference is likely due to N-myristoylation of BSK1 (26). N-myristoylation occurs co-translationally and its catalytic enzymes have been associated with the ER in addition to cytosol (48, 49). Co-translational N-myristoylation would allow BSK1 to be inserted at the ER membrane, which follows anterograde trafficking through the Golgi apparatus to the TGN/EE, where PATs are localized and *S*-acylation of BSK1 occurred (Fig. 8). Similar situation was reported for *h*-type thioredoxin (*h*-TRX), N-myristoylation alone confers its localization to the ER/Golgi whereas *S*-acylation is required for its localization to the PM (50). It may be a general mechanism for proteins whose PM targeting depends on both N-myristoylation and *S*-acylation, which are many (25).

Unlike the TGN/EE-associated distribution of BSK1$^{CC3/4SS}$-GFP in wild type, BSK1-GFP was still associated with the PM in the *PAT* triple mutants, albeit at a significantly reduced abundance (Fig. 8). The difference may be due to further redundancy among other PATs (6), which could compensate for the loss of *PAT19*, *PAT20*, and *PAT22*. Consistently, BSK1-GFP still shows a certain level of *S*-acylation in the *PAT* triple mutants (Fig. 6). In addition, overexpressing BSK1 but not BSK1$^{CC3/4SS}$ rescues the defects of the *PAT* triple mutants (Fig. 7), indicating a remaining activity of BSK1 despite functional loss of *PAT19*, *PAT20*, and *PAT22*.

Materials and Methods

Plant Growth and Transformation. *Arabidopsis thaliana* Columbia-0 ecotype was used as the wild type for all experiments. The T-DNA insertion line SAIL_767_E09.v1 (*pat19-1*), SALK_138998 (*pat20-1*), and WiscDsLox476D04 (*pat22-1*) were obtained from the Arabidopsis Biological Resource Center (www.arabidopsis.org). *pat19-2, pat19-3, pat20-2, and pat22-2* were generated by CRISPR-Cas9. The *pat1;2;3;4;8* mutant (Xiang et al., accompany manuscript) and the *PAT4g:GFP;pat4* transgenic line (10) were described. Plants were grown as described (4). Stable transgenic plants were selected on half-strength (1/2) MS medium supplemented with 30 μg/mL Basta salts (Sigma-Aldrich) or 25 μg/mL Hygromycin (Roche).

DNA Manipulation. All constructs were generated using the Gateway technology (Invitrogen) except for the CRISPR/Cas9 constructs. Entry vectors containing gene-specific sequences were generated in pENTR/SD/D-TOPO (Invitrogen) with the following primer pairs: P400/P401 for the *PAT19* promoter, ZP6588/ZP6739 for the *PAT20* promoter, ZP8620/ZP6741 for the *PAT22* promoter, and ZP6588/ZP6589 for the *PAT20* genomic fragment. Then the entry vectors were combined with the destination vector GW:GUS (4, 36) to generate corresponding expression vectors *pPAT19*:GUS, *pPAT20*:GUS, and *pPAT22*:GUS. The *PAT20* genomic entry vectors were used in LR reactions with the destination vector GW:GFP (4) to generate the GFP-translational fusion construct *PAT20g*:GFP. The full-length coding sequences (CDS) of *PAT19*, *PAT20,* and *PAT22* were amplified by using the primer pair ZP6792/ZP6793, P398/P399, and ZP6798/ZP6799, respectively. The entry vectors were used in LR reactions with the destination vector *UBQ10*:GW-GFP (51) to generate the expression vectors *UBQ10:PAT19-GFP, UBQ10:PAT20-GFP*, and *UBQ10:PAT22-GFP*, respectively.

The CRISPR construct used to generate the *pat19;pat20;pat20* triple mutants was as described (52). Briefly, the target sites for *PAT19*, *PAT20*, and *PAT22* were selected using an online bioinformatics tool (http://www.genome.arizona.edu/crispr/CRISPRsearch.html) (53) and were incorporated into forward and reverse PCR primers. The *TRIPLEPAT*-CRISPR cassette was generated by PCR amplifications from pCBC-DT1T2 (53, 54) with the primer pairs ZP5183/ZP5184/ZP5185/ZP5186. The PCR products were digested with *Bsa*I and inserted into pHSE401 (54), resulting in pHSE401-*PAT19*/*PAT20*/*PAT22*. To verify that the CRISPR-Cas9 construct resulted in the genomic editing of *PAT19*, *PAT20*, and *PAT22*, the primer pair ZP5583/ZP5584 was used to amplify the *PAT19* genomic fragment of CRISPR-Cas9-transformed plants and the PCR fragments were sequenced with the primer ZP5583; the primer pair ZP5585/ZP5586 was used to amplify the *PAT20* genomic fragment of CRISPR-Cas9-transformed plants and the PCR fragments were sequenced with the primer ZP5585; the primer pair ZP5587/ZP5588 was used to amplify the *PAT22* genomic fragment of CRISPR-Cas9-transformed plants and the PCR fragments were sequenced with the primer ZP5587.

For vectors used in in vitro pull-down assays, PCR fragments of PAT19^{DHHC} (residue 67–224), PAT20^{DHHC} (residue 65–219), and PAT22^{DHHC} (residue 66–207) were amplified from entry vectors containing the corresponding CDS with the primer pair P3151/P1745, P3152/P3153, and P3154/P3155, respectively. The resultant PCR fragments were inserted into the destination vector pET-32a (55) pre-digested with *Bam*HI/*Sal*I using the pEASY-Uni Seamless Cloning and Assembly Kit (TRAN) to generate vectors expressing His-PAT19^{DHHC}, His-PAT20^{DHHC}, or His-PAT22^{DHHC}. GST-BSK1 was generated by combining the PCR fragment of *BSK1* amplified with the primer pair P631/P632 and linearized pEGX-4T-1 (56) with *Bam*HI/*Xho*I using the pEASY-Uni Seamless Cloning and Assembly Kit (TRAN).

All PCR amplifications were performed with Phusion hot-start high-fidelity DNA polymerase with the annealing temperature and extension times recommended by the manufacturer (Thermo Fisher Scientific). Entry vectors were sequenced, and sequences were analyzed using Vector NTI. All primers are listed in *SI Appendix*, Table S1.

Genotyping PCR, RNA Extraction, RT-PCRs and RT-qPCRs. The primers used to characterize mutants are as followed: ZP10247/ZP10248 for the wild-type copy and ZP10247/ZP4 for the mutant copy of *PAT19* in *pat19-1*; ZP10249/ZP10250 for the wild-type copy and ZP10249/ZP1 for the mutant copy of *PAT20* in *pat20-1*;

ZP8534/ZP8535 for the wild-type copy and ZP8534/ZP3 for the mutant copy of *PAT22* in *pat22-1*.

Total RNAs were isolated by using a Qiagen RNeasy plant mini kit according to the manufacturer's instructions. Oligo (dT)-primed cDNAs were synthesized by using SuperScript III reverse transcriptase with on-column DNase digestion (Invitrogen). For RT-PCR and qPCRs of *PAT19*, *PAT20*, and *PAT22* at diverse tissues, total RNAs were isolated from roots and seedlings at 7 DAG, leaves at 14 DAG, stems at 25 DAG, inflorescences at 4 to 5 d after anthesis, siliques at 12 d after fertilization, and open flowers. Primers used in RT-PCRs and RT-qPCRs are the following: ZP6498/ZP6499 for *PAT19*, ZP6500/ZP6501 for *PAT20*, ZP6504/ZP6505 for *PAT22*, NKP226/NKP227 for *DWF4*, and NKP240/NKP241 for *SAUR-AC1*. The RT-qPCRs were performed with the Bio-Rad CFX96 real-time system using SYBR Green real-time PCR master mix (Toyobo) as described (4). Primers for *GAPDH* and *ACTIN2* in RT-PCRs and qPCRs were as described (4). Analyses of transcript abundances were performed using Prism 7 (GraphPad Software). All primers are listed in *SI Appendix*, Table S1.

GUS Histochemistry. Seedlings at 4 DAG, leaves from 20 DAG plants, leaf epidermal cells, inflorescences, open flowers, and mature pollen grains were incubated for 4 h at room temperature in the dark with 5-bromo-4-chloro-3-indolyl-D-Glc UA (X-Gluc) before imaging (4, 57). Images were captured with an Olympus BX53 microscope or an Olympus SZX16 microscope as described (4, 57).

Fluorescence Microscopy and Pharmacological Treatment. Fluorescent images were captured using a Zeiss LSM 880 confocal laser scanning microscope (CLSM) with a 40/1.3 oil objective. GFP-RFP double-labeled materials were captured alternately using line-switching with the multi-track function (488 nm for GFP and 561 nm for RFP). Fluorescence was detected using a 505- to 550-nm filter for GFP or a 575- to 650-nm band-pass filter for RFP. Image processing was performed with the Zeiss LSM image processing software (Zeiss). PI staining was captured using the 600 to 650 nm for PI staining (58).

Stock solutions of BFA, FM4-64, 2-BP, cycloheximide (CHX), and brassinolide (BL) were prepared using DMSO as the solvent at the concentration of 35 mM, 4 mM, 10 mM, 50 mM, and 100 m$\mathbf{M}$, respectively. Stock solutions were diluted and added to 1/2 MS medium at the final concentrations of 50 μM BFA, 4 μM FM4-64, 20 μM 2-BP, 50 μM CHX, and 100 nM BL. DMSO was equally diluted as the controls. Seedlings at 4 DAG were dipped in liquid one-half-strength MS medium supplemented with 4 μM FM4-64 (Invitrogen) for 5 min (except for the 1 min assay) at room temperature. Seedlings were then washed three times with liquid 1/2 MS medium and treated with 50 μM BFA for 50 min prior to confocal fluorescence imaging (51). For PI staining, seedlings at 4 DAG were dipped in liquid 1/2 MS medium supplemented with PI for 1 min at room temperature as described (58).

For BL treatment on hypocotyl elongation and root growth, sterilized seeds were grown on one-half-strength MS plates containing 100 nM BL for 5 d or 7 d under dark for hypocotyl length or root length, respectively. Images of seedlings were captured by using an Olympus SZX16 microscope (22, 38). In total, 100 to 150 hypocotyls or primary roots for each genotype were quantified by using ImageJ. All experiments were repeated at least three times.

For BL treatment on PAT-GFP targeting, seedlings at 4 DAG were dipped in liquid 1/2 MS medium supplemented with 100 nM BL for 2 h at room temperature before imaging (22). For BL and ConcA treatment, 4 DAG seedlings were incubated in 1 mL of liquid 1/2 MS medium containing 100 nM BL and 2 μM ConcA at room temperature for 2 h before imaging (59). For BL and E-64d treatment, seedlings at 4 DAG were dipped in liquid 1/2 MS medium supplemented with 100 nM BL and 10 μM E64d at room temperature for 3 h before imaging.

For 2-BP treatment, seedlings at 4 DAG were dipped in liquid 1/2 MS medium supplemented with 20 μM 2-BP or DMSO for 12 h at room temperature before imaging, as described (3, 51). For CHX and BFA treatment, seedlings of 4 DAG were pre-incubated for 30 min in liquid 1/2 MS medium supplemented with 50 μM CHX, then treated with 4 μM FM4-64 for 5 min, and then incubated in the medium with 50 μM CHX and 50 μM BFA for 50 min before imaging (60).

Phenotype Analysis. To analyze primary root length, seeds were treated as previously described (61) with slight modifications. Primary roots from 7 DAG seedlings were imaged and measured using the ImageJ software (http://rsbweb.nih.gov/ij/). In total, 90 to 100 roots for each genotype were measured and quantified. Statistical analyses were performed by one-way ANOVA (Tukey's multiple comparisons test).

For stomatal analysis, rosette leaves from 3 WAG plants were used to measure stomatal density. The number of stomata was counted from abaxial epidermis at the midpoint of the leaf lamina on the midrib and margin. The abaxial epidermis was photographed by using a ZEISS AXIO Observer fluorescence microscope. Stomatal density was quantified by using ImageJ. Experiments were repeated three times with similar results. Statistical analyses were performed by one-way ANOVA (Tukey's multiple comparisons test).

To examine hypocotyl elongation, seeds were treated at 4 °C for 2 d and incubated under light at 22 °C for 8 h before being placed in the dark for 5 d on one-half-strength MS medium to promote germination before growing in the dark. About 150 hypocotyls for each genotype were measured using ImageJ. One-way ANOVA (Tukey's multiple comparisons test) was performed with build-in analysis for the length of hypocotyls.

Protein Interaction Assays. For split-luciferase complementation assays, the destination vectors *pCAMBIA1300-35S-GW-cLUC* and *pCAMBIA1300-35S-GW-nLUC* were used to generate the expression vectors, including *pCAMBIA1300-35S-PAT19-cLUC*, *pCAMBIA1300-35S-PAT20-cLUC*, *pCAMBIA1300-35S-PAT22-cLUC*, *pCAMBIA1300-35S-BSK1-nLUC*, and *pCAMBIA1300-35S-CDG1-nLUC*. *Agrobacterium tumefaciens* (GV3101) cells transformed with indicated expression vectors were infiltrated into leaves of *N. benthamiana* at 4 wk after germination (WAG). Infiltrated leaves were then incubated at room temperature for 48 h, surfaced sprayed with 1 mM D-luciferin, incubated in the dark for 5 to 10 min to allow the chlorophyll luminescence to decay as described (52, 62). LUC signals were then detected by using Chemiluminescence imaging analysis system (FUSION-PULSE 6).

For FRET assays, the vectors *35S:BSK1-GFP*, *35S:BRI1-mCherry*, and *35S:mCherry* were performed in Arabidopsis protoplasts by transient transformations as described (52). The calculation of FRET efficiency is as described (52, 63, 64).

The mbSUS assays were performed by using Yeastmaker™ Yeast Transformation System 2 (Clontech) as described in the User Manual (PT1172-1, Clontech) (40). The full-length CDS for *PAT19*, *PAT20*, and *PAT22* were cloned into pBT3-N vector while the full-length CDS for *BSK1* and *CDG1* were cloned into pPR3-N vector. Different combinations of bait and prey vectors were co-transformed into the yeast strain NMY51. Clones were then selected on quadruple-dropout medium lacking leucine, tryptophan, histidine, and adenine (-WLHA) for 3 d at 30 °C to assay positive interactions.

For in vitro pull-down assays, the recombinant vectors containing *His-PAT19^{DHHC}*, *His-PAT20^{DHHC}*, *His-PAT22^{DHHC}*, or *GST-BSK1* were transformed into BL21 competent cells (DE3), cultured at 37 °C in Luria–Bertani (LB) medium at the presence of antibiotics (100 mg/mL ampicillin) to an OD600 of 0.6 to 0.8. Protein expression was induced by adding 0.8 mM isopropyl-b-D-1thiogalactopyranosid (IPTG). Cells were further incubated in a horizontal shaker with slow shaking overnight at 16 °C for 12 to 18 h. The recombinant proteins were affinity-purified according to the manufacturer's protocol (GE Healthcare Life Science) and analyzed by sodium dodecyl sulfate polyacrylamide gel electrophoresis (SDS-PAGE) as described (55). In vitro pull-down assays were performed as described (52, 55, 56).

The Acyl-RAC Assay. The acyl-RAC assay was performed as described (17) with slight modifications. Seedlings at 10 DAG were pulverized in liquid nitrogen, suspended in Lysis buffer (100 mM HEPES pH7.5, 1 mM EDTA, and proteinase inhibitor cocktail), and centrifuged 60 min at 15,871×*g* at 4 °C. The protein concentration of different samples was detected by the BCA method. A mixture of 833 μg protein sample and 250 μL blocking buffer (100 mM HEPES, 1 mM EDTA, 5% SDS, and 25 mM NEM) was incubated at 45 °C for 10 min. Then, samples were added with triploid pre-cooled acetone and precipitated at −20 °C for over 20 min. Following centrifugation at 2,348×*g* for 10 min, the pellet was washed by 70% cold acetone. After the removal of acetone, the pellet was resuspended in 1 mL binding buffer (100 mM HEPES, 1 mM EDTA, and 1% SDS, pH7.5). The suspension was divided into two equal parts and each was mixed with 50 μL pre-washed thiopropyl Sepharose and 67 μL of either 2 M NH_2OH (pH7.5) or 2 M NaCl (as control). Then, 80 μL of the mixtures from the positive (NH_2OH) or negative (NaCl) was saved as total inputs. The mixtures with sepharose were incubated for binding reaction on a rotator at room temperature for 3 h. Then, the sepharose

beads were washed five times with binding buffer. Elution was performed using 125 μL elution buffer (100 mM HEPES, 1 mM EDTA, 1% SDS, and 50 mM DTT, pH7.5) at room temperature for 20 min. Following centrifugation at 100×*g* for 1 min, 120 μL supernatant was transferred to a new tube, and then resuspended in 1× protein loading buffer and heated at 100 °C for 10 min. Western blots were performed using anti-GFP antibodies (17).

Statistical Analysis. Quantification data are analyzed by using GraphPad Prism 6.02 (www.graphpad.com/scientific-software/prism/). All statistical analyses were performed with one-way ANOVA (Tukey's multiple comparisons test) with build-in analysis tools and parameters.

Accession Numbers. Arabidopsis Genome Initiative locus identifiers for the genes mentioned in this article are At4G39400 for *BRI1*, At4g35230 for *BSK1*, At1g75080 for *BZR1*, At3g26940 for *CDG1*, At2g40610 for *EXPA8*, At4g15080 for *PAT19*, At3g22180 for *PAT20*, At1g69420 for *PAT22*, At4g38850 for *SAUR-AC1*, and At3g50660 for *DWF4*.

Data, Materials, and Software Availability. All study data are included in the article and/or *SI Appendix*.

ACKNOWLEDGMENTS. We thank Prof. Jianbin Lai for BSK1^{C3S}-GFP seeds and Prof. Wenqiang Tang for constructive suggestions. This work was supported by Natural Science Foundation of China (31970332 to S.L.).

1. P. A. Hemsley, C. S. Grierson, Multiple roles for protein palmitoylation in plants. *Trends Plant Sci.* **13**, 295–302 (2008).
2. S. Baekkeskov, J. Kanaani, Palmitoylation cycles and regulation of protein function (Review). *Mol. Membr. Biol.* **26**, 42–54 (2009).
3. Y. L. Zhang *et al.*, Protein palmitoylation is critical for the polar growth of root hairs in *Arabidopsis*. *BMC Plant Biol.* **15**, 50 (2015).
4. L. Z. Zhou *et al.*, PROTEIN S-ACYL TRANSFERASE10 is critical for development and salt tolerance in *Arabidopsis*. *Plant Cell* **25**, 1093–1107 (2013).
5. J. Greaves, L. H. Chamberlain, DHHC palmitoyl transferases: Substrate interactions and (patho) physiology. *Trends Biochem. Sci.* **36**, 245–253 (2011).
6. O. Batistic, Genomics and localization of the Arabidopsis DHHC-cysteine-rich domain S-acyltransferase protein family. *Plant Physiol.* **160**, 1597–1612 (2012).
7. P. A. Hemsley, A. C. Kemp, C. S. Grierson, The TIP GROWTH DEFECTIVE1 S-acyl transferase regulates plant cell growth in *Arabidopsis*. *Plant Cell* **17**, 2554–2563 (2005).
8. E. Ryan, C. S. Grierson, A. Cavell, M. Steer, L. Dolan, *TIP1* is required for both tip growth and non-tip growth in *Arabidopsis*. *New Phytol.* **138**, 49–58 (1998).
9. B. Qi, J. Doughty, R. Hooley, A Golgi and tonoplast localized S-acyl transferase is involved in cell expansion, cell division, vascular patterning and fertility in Arabidopsis. *New Phytol.* **200**, 444–456 (2013).
10. Z. Y. Wan *et al.*, Arabidopsis PROTEIN S-ACYL TRANSFERASE4 mediates root hair growth. *Plant J.* **90**, 249–260 (2017).
11. X. Y. Zhao *et al.*, Precocious leaf senescence by functional loss of PROTEIN S-ACYL TRANSFERASE14 involves the NPR1-dependent salicylic acid signaling. *Sci. Rep.* **6**, 20309 (2016).
12. J. Lai *et al.*, Two homologous protein S-acyltransferases, PAT13 and PAT14, cooperatively regulate leaf senescence in *Arabidopsis*. *J. Exp. Bot.* **66**, 6345–6353 (2015).
13. Y. Li, R. Scott, J. Doughty, M. Grant, B. Qi, Protein S-acyltransferase 14: A specific role for palmitoylation in leaf senescence in Arabidopsis. *Plant Physiol.* **170**, 415–428 (2016).
14. Y. Li *et al.*, Protein S-acyl transferase 15 is involved in seed triacylglycerol catabolism during early seedling growth in Arabidopsis. *J. Exp. Bot.* **70**, 5205–5216 (2019).
15. D. Chen *et al.*, *S*-acylation of P2K1 mediates extracellular ATP-induced immune signaling in *Arabidopsis*. *Nat. Commun.* **12**, 2750 (2021).
16. P. A. Hemsley, T. Weimar, K. S. Lilley, P. Dupree, C. S. Grierson, A proteomic approach identifies many novel palmitoylated proteins in Arabidopsis. *New Phytol.* **197**, 805–814 (2013).
17. S. Chai, F. R. Ge, Y. Zhang, S. Li, S-acylation of CBL10/SCaBP8 by PAT10 is crucial for its tonoplast association and function in salt tolerance. *J. Integr. Plant Biol.* **62**, 718–722 (2020).
18. J. Gao, G. Huang, X. Chen, Y. X. Zhu, PROTEIN S-ACYL TRANSFERASE 13/16 modulate disease resistance by S-acylation of the nucleotide binding, leucine-rich repeat protein R5L1 in *Arabidopsis*. *J. Integr. Plant Biol.* **64**, 1789–1802 (2022).
19. T.-W. Kim *et al.*, Brassinosteroid signal transduction from cell-surface receptor kinases to nuclear transcription factors. *Nat. Cell Biol.* **11**, 1254–1260 (2009).
20. Y. Belkhadir, Y. Jaillais, The molecular circuitry of brassinosteroid signaling. *New Phytol.* **206**, 522–540 (2015).
21. B. Su *et al.*, Dynamic spatial reorganization of BSK1 complexes in the plasma membrane underpins signal-specific activation for growth and immunity. *Mol. Plant* **14**, 588–603 (2021).
22. W. Tang *et al.*, BSKs mediate signal transduction from the receptor kinase BRI1 in Arabidopsis. *Science* **321**, 557–560 (2008).
23. T. W. Kim, S. Guan, A. L. Burlingame, Z. Y. Wang, The CDG1 kinase mediates brassinosteroid signal transduction from BRI1 receptor kinase to BSU1 phosphatase and GSK3-like kinase BIN2. *Mol. Cell* **43**, 561–571 (2011).
24. J. Zhu *et al.*, Higher-ordered actin structures remodeled by *Arabidopsis* ACTIN-DEPOLYMERIZING FACTOR5 are important for pollen germination and pollen tube growth. *Mol. Plant* **10**, 1065–1081 (2017).
25. M. P. Running, The role of lipid post-translational modification in plant developmental processes. *Front. Plant Sci.* **5**, 50 (2014).
26. H. Shi *et al.*, BR-SIGNALING KINASE1 physically associates with FLAGELLIN SENSING2 and regulates plant innate immunity in *Arabidopsis*. *Plant Cell* **25**, 1143–1157 (2013).
27. X. Liu *et al.*, Salicylic acid attenuates brassinosteroid signaling via protein de-S-acylation. *EMBO J.* **42**, e112998 (2023), 10.15252/embj.2022112998.
28. Y. Li *et al.*, Both male and female gametogenesis require a fully functional protein *S*-acyl transferase 21 in *Arabidopsis thaliana*. *Plant J.* **100**, 754–767 (2019).
29. N. Geldner *et al.*, Rapid, combinatorial analysis of membrane compartments in intact plants with a multicolor marker set. *Plant J.* **59**, 169–178 (2009).
30. M. P. Gonzalez-Garcia *et al.*, Brassinosteroids control meristem size by promoting cell cycle progression in Arabidopsis roots. *Development* **138**, 849–859 (2011).
31. Y. Hacham *et al.*, Brassinosteroid perception in the epidermis controls root meristem size. *Development* **138**, 839–848 (2011).
32. S. Sreeramulu *et al.*, BSKs are partially redundant positive regulators of brassinosteroid signaling in Arabidopsis. *Plant J.* **74**, 905–919 (2013).
33. G. E. Gudesblat *et al.*, SPEECHLESS integrates brassinosteroid and stomata signalling pathways. *Nat. Cell Biol.* **14**, 548–554 (2012).
34. T.-W. Kim, M. Michniewicz, D. C. Bergmann, Z.-Y. Wang, Brassinosteroid regulates stomatal development by GSK3-mediated inhibition of a MAPK pathway. *Nature* **482**, 419–422 (2012).
35. T. M. Nolan, N. Vukasinovic, D. Liu, E. Russinova, Y. Yin, Brassinosteroids: Multidimensional regulators of plant growth, development, and stress responses. *Plant Cell* **32**, 295–318 (2020).
36. H. Y. Huang *et al.*, BR signal influences *Arabidopsis* ovule and seed number through regulating related genes expression by BZR1. *Mol. Plant* **6**, 456–469 (2013).
37. D. Jia *et al.*, Brassinosteroids regulate outer ovule integument growth in part via the control of *INNER NO OUTER* by BRASSINOZOLE-RESISTANT family transcription factors. *J. Integr. Plant Biol.* **62**, 1093–1111 (2020).
38. X. Y. Zhou, L. Song, H. W. Xue, Brassinosteroids regulate the differential growth of Arabidopsis hypocotyls through auxin signaling components IAA19 and ARF7. *Mol. Plant* **6**, 887–904 (2013).
39. B. C. Jennings *et al.*, 2-Bromopalmitate and 2-(2-hydroxy-5-nitro-benzylidene)-benzo[b]thiophen-3-one inhibit DHHC-mediated palmitoylation in vitro. *J. Lipid Res.* **50**, 233–242 (2009).
40. F. Xiong *et al.*, Hypocotyl elongation inhibition of melatonin is involved in repressing brassinosteroid biosynthesis in Arabidopsis. *Front Plant Sci.* **10**, 1082 (2019).
41. D. Scheuring *et al.*, Multivesicular bodies mature from the trans-Golgi network/early endosome in Arabidopsis. *Plant Cell* **23**, 3463–3481 (2011).
42. Y. Luo *et al.*, Deubiquitinating enzymes UBP12 and UBP13 stabilize the brassinosteroid receptor BRI1. *EMBO Rep.* **23**, e53354 (2022).
43. K. Yamada, K. Fuji, T. Shimada, M. Nishimura, I. Hara-Nishimura, Endosomal proteases facilitate the fusion of endosomes with vacuoles at the final step of the endocytotic pathway. *Plant J.* **41**, 888–898 (2005).
44. T. Li *et al.*, Brassinosteroids regulate root meristem development by mediating BIN2-UPB1 module in *Arabidopsis*. *PLoS Genet.* **16**, e1008883 (2020).
45. H. Ren *et al.*, BRASSINOSTEROID-SIGNALING KINASE 3, a plasma membrane-associated scaffold protein involved in early brassinosteroid signaling. *PLoS Genet.* **15**, e1007904 (2019).
46. Y. Jaillais, G. Vert, Brassinosteroid signaling and BRI1 dynamics went underground. *Curr. Opin. Plant Biol.* **33**, 92–100 (2016).
47. S. Martins *et al.*, Internalization and vacuolar targeting of the brassinosteroid hormone receptor BRI1 are regulated by ubiquitination. *Nat. Commun.* **6**, 6151 (2015).
48. J. A. Boutin, Myristoylation. *Cell Signal* **9**, 15–35 (1997).
49. B. Wang *et al.*, Protein N-myristoylation: Functions and mechanisms in control of innate immunity. *Cell Mol. Immunol.* **18**, 878–888 (2021).
50. J. A. Traverso *et al.*, Roles of N-terminal fatty acid acylations in membrane compartment partitioning: Arabidopsis h-type thioredoxins as a case study. *Plant Cell* **25**, 1056–1077 (2013).
51. Q. N. Feng *et al.*, Adaptor Protein-3-dependent vacuolar trafficking involves a subpopulation of COPII and HOPS tethering proteins. *Plant Physiol.* **174**, 1609–1620 (2017).
52. F. Liu *et al.*, The canonical α-SNAP is essential for gametophytic development in Arabidopsis. *PLoS Genet.* **17**, e1009505 (2021).
53. Z. P. Wang *et al.*, Egg cell-specific promoter-controlled CRISPR/Cas9 efficiently generates homozygous mutants for multiple target genes in Arabidopsis in a single generation. *Genome Biol.* **16**, 144 (2015).
54. H. L. Xing *et al.*, A CRISPR/Cas9 toolkit for multiplex genome editing in plants. *BMC Plant Biol.* **14**, 327 (2014).
55. E. Li *et al.*, AGC1.5 kinase phosphorylates RopGEFs to control pollen tube growth. *Mol. Plant* **11**, 1198–1209 (2018).
56. F. Xiong *et al.*, Arabidopsis KETCH1 is critical for the nuclear accumulation of ribosomal proteins and gametogenesis. *Plant Cell* **32**, 1270–1284 (2020).
57. J. G. Wang *et al.*, HAPLESS13, the Arabidopsis μ1 adaptin, is essential for protein sorting at the trans-Golgi network/early endosome. *Plant Physiol.* **162**, 1897–1910 (2013).
58. F. Xiong *et al.*, Transcriptional regulation of PLETHORA1 in the root meristem through an importin and its two antagonistic cargos. *Plant Cell* **32**, 3812–3824 (2020).
59. Zhang *et al.*, *Arabidopsis* R-SNARE proteins VAMP721 and VAMP722 are required for cell plate formation. *PLoS ONE* **6**, e26129 (2011).
60. F. R. Ge, S. Chai, S. Li, Y. Zhang, Targeting and signaling of Rho of plants guanosine triphosphatases require synergistic interaction between guanine nucleotide inhibitor and vesicular trafficking. *J. Integr. Plant Biol.* **62**, 1484–1499 (2020), 10.1111/jipb.12928.
61. S. Promchuea, Y. Zhu, Z. Chen, J. Zhang, Z. Gong, ARF2 coordinates with PLETHORAs and PINs to orchestrate ABA-mediated root meristem activity in Arabidopsis. *J. Integr. Plant Biol.* **59**, 30–43 (2017).
62. H. Chen *et al.*, Firefly luciferase complementation imaging assay for protein–protein interactions in plants. *Plant Physiol.* **146**, 368–376 (2008).
63. E. Li *et al.*, A positive feedback circuit for ROP-mediated polar growth. *Mol. Plant* **14**, 395–410 (2020), 10.1016/j.molp.2020.11.017.
64. X. Wang *et al.*, SKIP is a component of the spliceosome linking alternative splicing and the circadian clock in Arabidopsis. *Plant Cell* **24**, 3278–3295 (2012).